An Impact-Coupled MEMS Electrostatic Kinetic Energy Harvester and Its Predictive Model Taking Nonlinear Air Damping Effect Into Account

Yingxian Lu, Jérôme Juillard, Francesco Cottone, Dimitri Galayko, *Member, IEEE*, and Philippe Basset

***Abstract*— This paper describes a predictive and complete numeric model of a multi-mass and impact-coupled MEMS electrostatic kinetic energy harvester (e-KEH). A silicon resonator is coupled with elastic silicon beams (acting as a part of stoppers) and a miniature metallic ball. The model considers all these impacts as well as the electromechanical force and catches the frequency-up and spring-softening effects. More importantly, for the first time, it models accurately the evolving and non-linear squeeze-film air damping effect in a gap-closing transducer, which is induced by the large amplitude of displacement of the silicon mass. The predictions provided by the model are compared with experimental results, showing a good consistency. The key parameters of the KEH are analyzed with the proposed model, which can be of great help for further design optimization of similar devices. [2018-0174]**

***Index Terms*— MEMS modeling, electrostatic vibration energy harvester, impact-based frequency up conversion, nonlinear air damping.**

I. Introduction

KINETIC energy is abundantly existing in the environment, and is a possible localized source of energy for wireless communication nodes in sensor networks or wearable electronics. The ambient vibration and human motion are usually random signals featured with large bandwidth and low frequency. Kinetic energy harvesters (KEHs) are used to transduce the kinetic energy in vibrations or motion into electric energy. Resonant structure [1] is commonly applied to KEHs to benefit from mechanical amplification. However, it is not easy to reduce the resonance frequency of a small-sized KEH. To improve the output power at low frequency, mechanical nonlinearities are introduced in resonant KEHs, including bistability [2] or impact-coupled mechanical frequency up conversion [3], [4]–[6]. Frequency up conversion based on array structures is also applied in lots of designs [7]–[9]. Non-resonant structure including rolling movement is another solution to lower the working frequency [10], [11]. Other techniques improve the efficiency in different ways of mechanic-to-electric transduction. For electrostatic KEHs, to enhance the transduction efficiency it is necessary to increase the area of their QV cycles (the cycles of charge-voltage evolution of the device) [12]. Various approaches include reaching a large range of capacitance variation [13], applying a large bias voltage across the device [14], and applying conditioning circuits that lead to preferred geometry of QV cycles [15]. Among them, capacitance variations are realized through various ways through combining in-plane or out-of- plane motions and gap-closing or overlapping styles [5], [7], [16], [17]. Previously reported modeling work of capacitive KEHs usually emphasizes on the accuracy of capacitance estimation [18].

In our previous work, we proposed a low-frequency KEH based on impact-coupled mechanical frequency up conversion technique, which reaches a large range of capacitance variation through an in-plane gap-closing interdigital comb structure [19]. The prototype consists of a spring-mass structure with elastic stoppers and an impact-coupled miniature ball. Two impact mechanisms are implemented: the movable mass impacting with the ball and with the stoppers. The variable capacitance of the KEH is realized by an in-plane gap-closing interdigital comb structure. The device is well adapted to low frequency operations thanks to the impact mechanisms, and the mass displacement reaches the upper limit (determined by the stoppers) even at low frequencies.

The air damping effect is a key factor that influence the maximum capacitance of the electrostatic transducer [19], and thus very important in the prototype modeling. In one of our previous work [20], we used linear air damping assumption as proposed in [21], which is accurate only for small displacement, and thus is consistent with experimental results only when the excitation levels are low. With high level excitations,

Manuscript received July 30, 2018; revised September 20, 2018; accepted October 13, 2018. Date of publication October 26, 2018; date of current version November 29, 2018. Subject Editor C. Rembe. *(Corresponding author: Philippe Basset.)*

Y. Lu was with Université Paris-Est/ESYCOM/CNAM, ESIEE Paris & UPEMLV, 93162 Noisy-le-Grand, France. She is now with Tsinghua University, Beijing 100084 , China (e-mail: yingxianlu@tsinghua.edu.cn).

J. Juillard is with GEEPS-UMR8507-CNRS-CentraleSupélec-Université Paris-Sud-Université Pierre et Marie Curie, 91190 Gif-sur-Yvette, France (e-mail: jerome.juillard@geeps.centralesupelec.fr).

F. Cottone was with Université Paris-Est/ESYCOM/CNAM, ESIEE Paris & UPEMLV, 93162 Noisy-le-Grand, France. He is now with the Department of Physics, University of Perugia, 06100 Perugia, Italy (e-mail: francesco.cottone@unipg.it).

D. Galayko is with the LIP6 Laboratory, CIAN Group, Sorbonne Université, 75005 Paris, France (e-mail: dimitri.galayko@lip6.fr).

P. Basset is with Université Paris-Est/ESYCOM/CNAM,ESIEE Paris & UPEMLV, 93162 Noisy-le-Grand, France (e-mail: p.basset@esiee.fr).

Color versions of one or more of the figures in this paper are available online at http://ieeexplore.ieee.org.

Digital Object Identifier 10.1109/JMEMS.2018.2876353

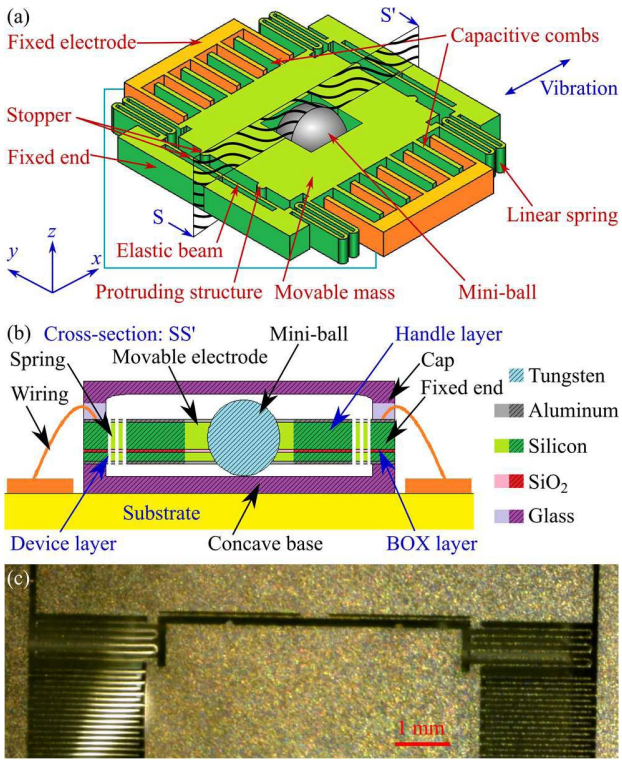

Fig. 1. Demonstration of the impact-coupled low frequency kinetic energy harvester (a) 3D view (b) cross-section view (c) microscopic photograph.

the nonlinear air damping effect in MEMS KEHs must be taken into account [13]. In [22], the nonlinear air damping is modeled through post-fabrication fitting technique to achieve good consistency with experiments. Indeed, the squeeze-film air damping force in a gap-closing comb structure increases dramatically with the size reduction of the air gap between electrodes. Thus the influences of the position of the movable electrode must be considered to achieve a more accurate model. However, such models are not predictive: they must fully rely on the post-fabrication measurements.

This paper presents a predictive and more accurate model than our previous work [20], by continuously calculates the squeeze-film air damping force according to the size of the varying air gap. It also takes into account the impacts within the prototype, so that the power output capacity of the prototype with a given excitation can be estimated through simulations of transient output signal. The device's capacitance variation under sinusoidal excitation is simulated against frequency sweeps, and its output power is obtained accordingly. In the next section, the modeled prototype is presented with detailed design parameters. Then the physical and numerical aspects are described in sections III and IV. In section V, the experimental measurements of the prototype are compared with predictions of simulations for validation of the model. Parametric study is carried out with several design parameters in section VI for performance optimization of the KEH.

II. Principle of Device

The object of this study is a MEMS KEH design based on a bulk etching process of an SOI wafer [23], which implements gap-closing combs as the capacitive structure. The schematic and the microscopic photograph of the prototype are shown in fig 1. The cardinal structure of the prototype is contained in a cavity surrounded by a concave base, fixed structures along the edges and a pre-etched cap. A movable electrode is suspended in the cavity, linked to fixed ends through linear springs. At the center of the movable electrode there is a through-hole holding a miniature ball of tungsten. On the two fixed ends along the vibration direction are elastic stoppers confining the displacement of the movable electrodes. Capacitive structure of the prototype is along the other two fixed edges, with a form of in-plane gap-closing interdigital comb structure [23]. The movable electrode is biased to a DC voltage through either an external voltage or a pre-charged electret. The resonant frequency of the mass-spring system in the design is around 100 Hz. With an excitation of low frequency (below 100 Hz), the ball easily moves relative to the device case due to inertia, impacting on the movable electrode. Thus the oscillation of the movable electrode at resonant frequency (higher than the excitation frequency) is triggered, resulting in a capacitance variation of the prototype. The device is then able to generate an AC signal between its two electrodes. Design parameters of the prototype can be found in Table I.

TABLE I
Design Parameters of the Prototype.

Quantity	Symbol	Value
Thickness of handle layer	T_1	380 µm
Thickness of device layer	T_2	100 µm
Thickness of BOX layer	T_{ox}	2 µm
Mass of movable electrode	m	77.5 mg
Mass of the miniature ball	m_b	32 mg
Initial gap between electrodes (defined in the mask)	G	70 µm
Initial gap of the stoppers	g_{st}	68 µm
Overlapping length of combs	L	1.9 mm
Number of movable combs	N_c	100
Cavity length	L_{cav}	3 mm
Radius of the miniature ball	r	0.8 mm

III. An Overview: A Model of the Device

To investigate the performance of the device under various conditions with varied design parameters, a model based on finite difference time domain method is developed, which takes into account the forces including the impacts and the nonlinear air damping. The model deals with a time-dependent excitation signal and relates it to the states of the KEH. It successively calculates the instantaneous status of the movable electrode and the mini-ball (the positions and the velocities) in chronological order, based on the excitation and arbitrary initial conditions. The model takes into account not only the linear forces, but also nonlinear effects including air damping and collisions.

A general flow chart of the process establishing and using the model is shown in fig. 2. The physical model is firstly studied and simplified, and a numeric model based on the

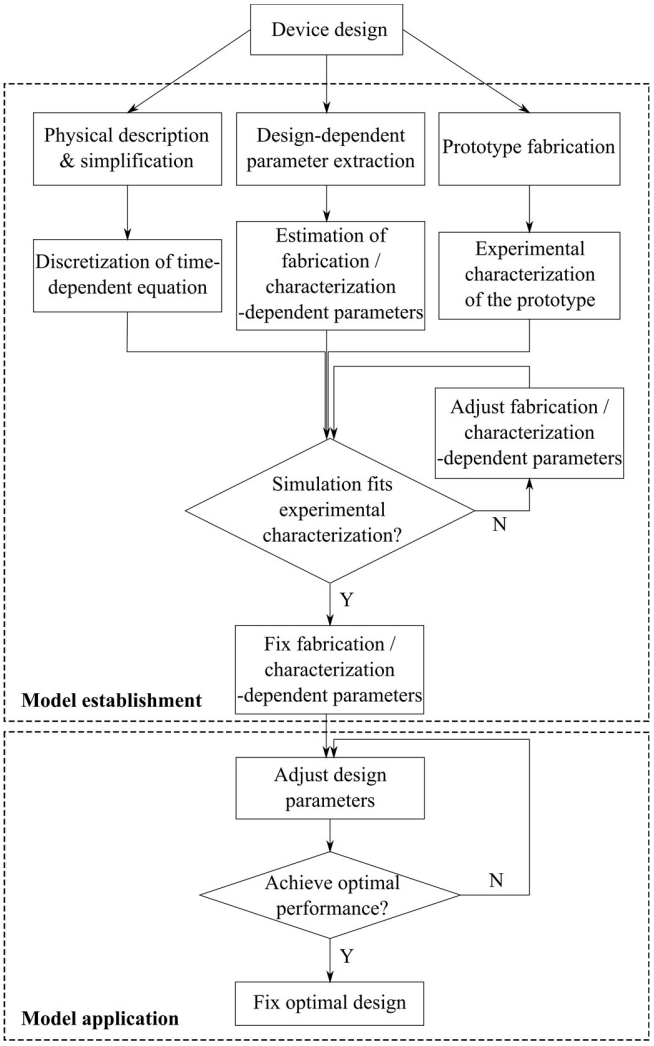

Fig. 2. A general flow chart to establish and use the model.

physical model is established. The model requires a group of parameters, either related to the design or to the fabrication and characterization. The former ones are obtained directly from the design, while the latter ones are adjusted according to one set of power measurement with the real device.

Unlike the previously reported models that needs adjustment of characterization-dependent parameters where the parameter needs to be adjusted each time the level of excitation varies, the model we introduce needs only one adjustment to determine a set of characterization-dependent parameters for all levels of excitation. In fact, the proposed model is suitable for all possible design parameters and all kinds of excitations, as long as the fabrication and characterization techniques remain unchanged. Once the experiment-dependent parameters are determined, the model can be used simply by changing the design parameters for the optimization purpose.

IV. Device Model: Physical

The device is modeled as a variable capacitor biased by a DC voltage, the capacitance of which is dependent on the position of its movable electrode. The calculation of the device

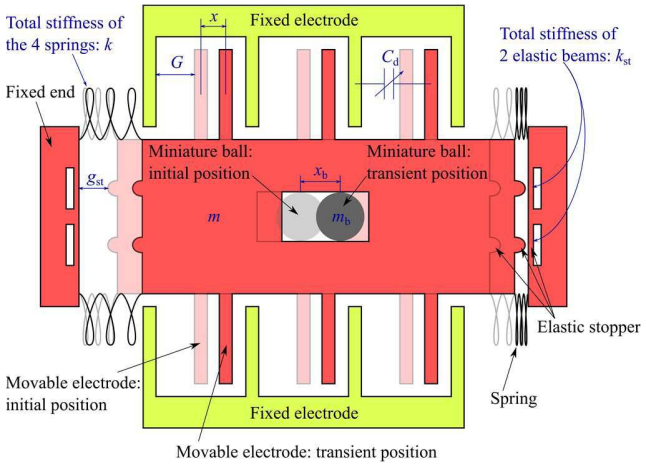

Fig. 3. A simplified schematic of the target prototype with demonstrations of the key variables and design parameters used in the model.

output signal is based on the capacitance variation and the load in connection to the KEH (either resistive load or AC/DC rectifying module). The performance of the device can then be predicted with a well-chosen time step in the transient simulation. A global view of the major variables applied in the model is demonstrated in fig 3.

A. Kinematic Equations

The forces acting on the movable electrode include the forces from the linear springs (F_{spr}) and the stoppers (F_{st}), the electrostatic force (F_{elec}), and the air damping force (F_{air}). The kinematic equation of the movable electrode is expressed as:

$$m\ddot{x} = -ma_{ext} + F_{spr} + F_{st} + F_{elec} + F_{air} \tag{1}$$

where m is the mass of the movable electrode; x, $\dot{x}$ and $\ddot{x}$ are its position, velocity and acceleration respectively, a_{ext} is the excitation acceleration. A sinusoidal signal $a_{ext} = A\sin(2\pi ft)$ is applied to the KEH in the experiments, where A and f are the amplitude and the frequency of acceleration.

The spring force is linear with displacement:

$$F_{spr} = -kx \tag{2}$$

where k is the total stiffness coefficient of the four springs. The force from the elastic stoppers is given by:

$$F_{st} = \begin{cases} 0, & |x| < g_{st} \\ -k_{st}\left(|x| - g_{st}\right)\mathrm{Sgn}\left(x\right), & |x| \geq g_{st} \end{cases} \tag{3}$$

where g_{st} is the initial size of the gap between the movable electrode and the stoppers. k_{st} is the total stiffness of the stoppers, while $\mathrm{Sgn}(\cdot)$ is the sign function.

The electrostatic force is related to the capacitance C and the charge on the electrodes q [24]:

$$F_{elec} = \frac{1}{2}\left(\frac{q}{C}\right)^2 \frac{\mathrm{d}C}{\mathrm{d}x} \tag{4}$$

where C is dependent only on x.

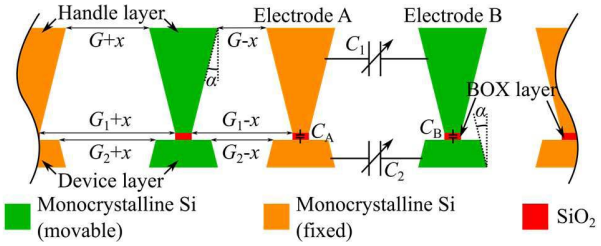

Fig. 4. Schematic of the capacitances within the SOI-based prototype and the tilt angle of sidewall caused by the DRIE fabrication.

The first derivative of charge with respect to time ($\dot{q}$) is related to the bias voltage V_{bias} and the load resistance R_{l}:

$$\dot{q} = \frac{1}{R_{\text{l}}}\left(-\frac{q}{C} + V_{\text{bias}}\right) \tag{5}$$

On the other hand, the kinematic equation of the miniature ball taking friction into account is described as:

$$m_{\text{b}}\ddot{x}_{\text{b}} = -m_{\text{b}}a_{\text{ext}} + F_{\text{friction}} \tag{6}$$

where m_{b} and x_{b} are the mass and position of the ball, while F_{friction} is the friction force from the framework of the device.

$$F_{\text{friction}} = \begin{cases} -\mu_{\text{f}} m_{\text{b}} g \,\text{Sgn}\,(\dot{x}_{\text{b}}) & \dot{x}_{\text{b}} \neq 0 \\ -m_{\text{b}} \cdot \min\left(\mu_{\text{f}} g, |a_{\text{ext}}|\right) \text{Sgn}\,(a_{\text{ext}}) & \dot{x}_{\text{b}} = 0 \end{cases} \tag{7}$$

herein μ_{f} is the coefficient of friction, g is gravity acceleration.

The kinematic equation of the miniature ball is valid when it does not contact with the movable electrode: $|x - x_{\text{b}}| < \Delta X$. Here ΔX is determined by the cavity length L_{cav} and the size of the ball (r as radius):

$$\Delta X = \frac{L_{\text{cav}}}{2} - r \tag{8}$$

B. Capacitance Variation

The capacitance C in equation (4) consists of the device capacitance and a parasitic capacitance C_{p} introduced by the packaging and the external electronics (unchanged with the motions of the harvester).

$$C = C_{\text{p}} + C_{\text{d}} \tag{9}$$

where C_{d} is the capacitance of the prototype. The capacitance are calculated with regard to the gap between electrodes (or to x), based on either analytic method or finite element method (FEM).

In the analytic calculation, the capacitance of the SOI-wafer-based device is given by:

$$C_{\text{d}} = C_1 + \frac{1}{\frac{1}{C_2} + \frac{1}{C_{\text{A}}} + \frac{1}{C_{\text{B}}}} \tag{10}$$

where C_1 and C_2 are the capacitances of the structures of the handle layer and the device layer respectively; while C_{A} and C_{B} are the capacitances of the oxide layer on electrodes A and B respectively, as shown in fig 4. The calculation of C_1 and C_2 considers the tilt angle of sidewall (α, also shown in fig 4) caused by the overetch during fabrication.

$$C_i = \frac{N_{\text{f}}\varepsilon_0 L}{2\tan\alpha} \ln\frac{G_i^2 - x^2}{G^2 - x^2}, i = 1 \text{ or } 2 \tag{11}$$

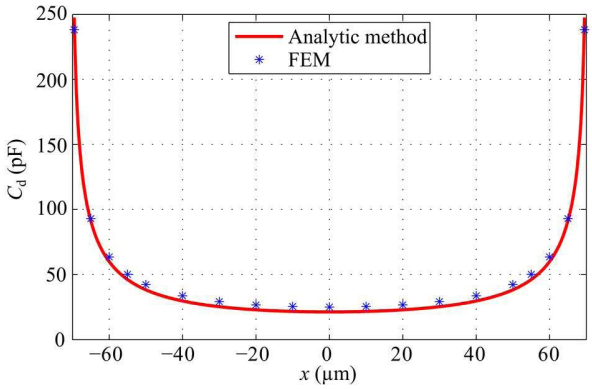

Fig. 5. The prototype capacitance C with respect to x (analytic method vs. FEM simulation). The sidewall angle $\alpha = 1.055°$ (see section IV for more details).

where N_{f} is the number of fingers on the movable electrode; ε_0 is the permittivity of vacuum (air); L is the overlapping length of combs. G_1 and G_2 are the initial gaps between electrodes on the handle layer and device layer caused by over-etching.

$$G_i = G + 2T_i \tan\alpha, \quad i = 1 \text{ or } 2 \tag{12}$$

While the two oxide-layer capacitances are obtained by:

$$C_{\text{A}} = \frac{\varepsilon_0\varepsilon_{\text{r}}}{T_{\text{ox}}} S_{\text{A}} \tag{13}$$

$$C_{\text{B}} = \frac{\varepsilon_0\varepsilon_{\text{r}}}{T_{\text{ox}}} S_{\text{B}} \tag{14}$$

where ε_{r} is the relative permittivity of silicon dioxide; T_{ox} is the thickness of the oxide layer; S_{A} is the area of the movable electrode; while S_{B} is the total area of the fixed electrodes.

The capacitance variation given by the FEM analysis is obtained through simulation with COMSOL Multiphysics, and compared with the analytical results so as to confirm the validity of the capacitance calculation of the analytic model, as shown in fig 5. The prediction of the analytical method is about 3 pF lower than the results given by the FEM prediction, but the error it brings to the current or power prediction is negligible.

C. Squeeze-Film Air Damping

The air damping model is developed from the nonlinear Reynolds equation for compressible air film [25]:

$$\frac{\partial}{\partial x}\left(P\frac{h^3}{\mu}\frac{\partial P}{\partial x}\right) + \frac{\partial}{\partial y}\left(P\frac{h^3}{\mu}\frac{\partial P}{\partial y}\right) + \frac{\partial}{\partial z}\left(P\frac{h^3}{\mu}\frac{\partial P}{\partial z}\right) = 12\frac{\partial(hP)}{\partial t} \tag{15}$$

where P is the pressure in the gas film; μ represents the coefficient of viscosity of the fluid; h is the thickness of the film; t is the time. x, y and z are the axes shown in fig 1a: x is the axis of mass displacement, y is the axis along the comb fingers, z is the thickness of the silicon wafer. Herein the inertia effect of the air and the temperature variation are neglected.

Since the influence of the over-etching sidewalls on the air damping effect is less significant than its influence on the capacitance variation [26], we simplify the air damping model by neglecting the sidewall angle, considering an air film with the uniform thickness h which is equivalent to the average thickness of the real air film. In addition, the viscosity coefficient of the air (μ) is considered uniform everywhere.

To simplify the equation, we neglect the pressure difference along x (Hypothesis 1, uniform pressure across the gap), and assume that the pressure proceeds a small variation p around the ambient pressure P_a ($p \ll P_a$, Hypothesis 2, small pressure variation), while assuming $\frac{12\mu}{h^2 P_a}\frac{\partial p}{\partial t} \ll \Delta p$ (Hypothesis 3, slow pressure variation). The simplified Reynolds equation based on the hypotheses above becomes:

$$\left(\frac{\partial^2}{\partial y^2}+\frac{\partial^2}{\partial z^2}\right)p=\frac{12\mu}{h^3}\frac{\partial h}{\partial t} \tag{16}$$

The following open boundary conditions are applied for solving the differential equation:

$$\begin{cases} p|_{y=-\frac{L}{2}\text{or}\frac{L}{2}}=0 \\ p|_{z=-\frac{T}{2}\text{or}\frac{T}{2}}=0 \end{cases} \tag{17}$$

where $T = T_1 + T_2 + T_{OX}$ is the thickness of the wafer. Taking the boundary conditions into account, the solution has the following approximated form:

$$p=\sum\nolimits_{\text{odd}k,l} a_{kl}\cos\frac{k\pi y}{L}\cos\frac{l\pi z}{T} \tag{18}$$

where the coefficient a_{mn} is the given by:

$$a_{mn}=-\frac{48\mu}{h^3}\frac{\partial h}{\partial t}\frac{Sa\left(\frac{m\pi}{2}\right)Sa\left(\frac{n\pi}{2}\right)}{\left(\frac{m\pi}{L}\right)^2+\left(\frac{n\pi}{T}\right)^2} \tag{19}$$

herein $Sa(\cdot)$ is the sampling function $Sa(\varphi) = \sin\varphi/\varphi$. While the thickness of the air films on the two sides of each comb is:

$$\begin{cases} h_1=\tilde{G}-x \\ h_2=\tilde{G}+x \end{cases} \tag{20}$$

where $\tilde{G}$ is the average thickness of the initial air film:

$$\tilde{G}=G+\frac{T_1^2+T_2^2}{T_1+T_2}\tan\alpha \tag{21}$$

The total air damping force acting on the movable mass is obtained:

$$F_{\text{air}}=N_c\int_{-\frac{T}{2}}^{\frac{T}{2}}\int_{-\frac{L}{2}}^{\frac{L}{2}}(p_2-p_1)\,\text{d}y\text{d}z=-d(x)\,\dot{x} \tag{22}$$

where N_c is the number of the combs on the movable electrode, p_1 and p_2 are the pressure on the two sides of one comb finger. while the expression of the damping coefficient is:

$$d(x)=c\left[\frac{1}{\left(1-x/\tilde{G}\right)^3}+\frac{1}{\left(1+x/\tilde{G}\right)^3}\right] \tag{23}$$

herein $c=\frac{768}{\pi^6}\frac{\mu T L N_c}{\tilde{G}^3}\sum\limits_{\text{odd}k,l}\frac{1/k^2l^2}{(k/L)^2+(l/T)^2}$ [27], which is only related to the dimensions of the comb fingers. The distribution

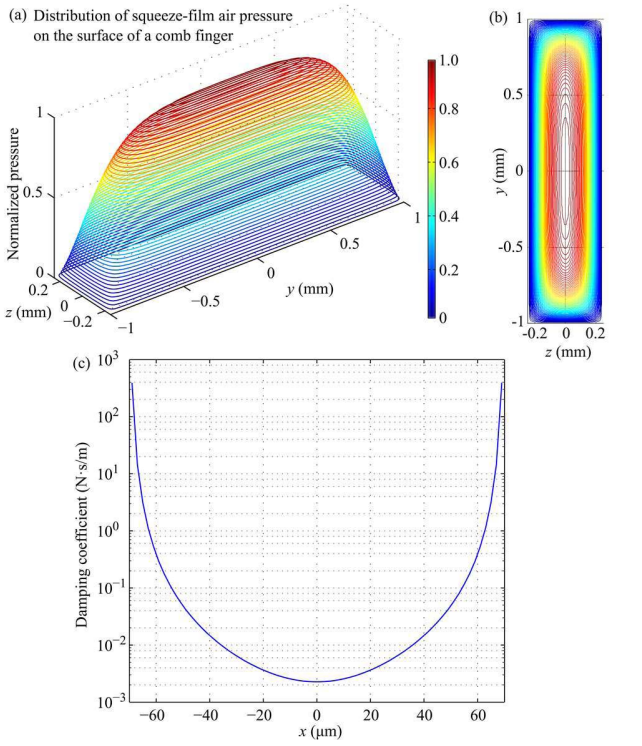

Fig. 6. (a-b) The pressure distribution (p) on a comb surface, normalized by its maximum value. (c) The overall squeeze-film air damping coefficient $d(x)$ in the prototype in relation with displacement x.

of normalized pressure (p_1 or p_2) on the comb (in regard to the maximum pressure on the surface) is shown in fig 6a-b. The maximum pressure is located at the center of the comb surface as expected. The total squeeze-film air damping coefficient of the whole device under standard atmospheric pressure is shown in fig 6c. The force is highly non-linear as expected.

D. Impact Detection

In other cases, there are impacts and separations between different parts of the device. The impacts and separations are inspected according to the current status (x_i, $x_{b,i}$) and the predicted status (x_{pr}, $x_{b,pr}$). The criteria for detecting these events are the following.

1) Impact With/Separation From the Stoppers: The movable electrode impacts with the stopper between t_i and t_{i+1} when

$$\begin{cases} |x_i| < g_{st} \\ |x_{pr}| > g_{st} \end{cases} \tag{24}$$

While separation from the stoppers occurs when

$$\begin{cases} |x_i| > g_{st} \\ |x_{pr}| < g_{st} \end{cases} \tag{25}$$

2) Impact With the Fixed Electrode: When the movable electrode is already in contact with the stopper at t_i, and the prediction for t_{i+1} exceeds the maximum possible displacement:

$$\begin{cases} g_{st} \le |x_i| < G \\ |x_{pr}| \ge G \end{cases} \tag{26}$$

3) Impact With the Ball: The impact between the ball and the movable mass occurs between t_i and t_{i+1} if

$$\begin{cases} \left|x_i - x_{\mathrm{b},i}\right| < \Delta X \\ \left|x_{\mathrm{pr}} - x_{\mathrm{b,pr}}\right| \geq \Delta X \end{cases} \tag{27}$$

E. Velocity Change With Impacts

According to the initial kinematic state of each continuously differentiable interval, the ending state can be deduced on the basis of the kinematic equations. At the inflection points (impacts and separations), the positions of the masses will keep the same, while the velocity changes follow the following rules. During any separations, we consider unchanged velocities by neglecting any additional force corresponding to the separations:

$$\dot{x}_{\text{after sep}} = \dot{x}_{\text{before sep}} \tag{28}$$

where $\dot{x}_{\text{before sep}}$ and $\dot{x}_{\text{after sep}}$ are the velocity of either the movable electrode or the miniature ball before and after any separation respectively.

The energy loss of the movable electrode during the impact with the stoppers is modeled as a velocity reduction that occurs right at the time of the impact:

$$\dot{x}_{\text{after imp}} = c_{\text{stop}} \cdot \dot{x}_{\text{before imp}} \tag{29}$$

where c_{imp} is the ratio of velocity change due to the energy loss brought by the impact. The motion of the movable electrode when it contacts with the fixed electrodes is considered as an immediate velocity reverse with a certain loss of energy:

$$\dot{x}_{\text{after imp}} = -c_{\text{stop}} \cdot \dot{x}_{\text{before imp}} \tag{30}$$

Because the duration of the movable electrode contacting with the fixed electrodes is much shorter than the duration it contacts with the stoppers. While the velocity change of the ball and the movable mass is also considered to occur immediately at the beginning of the contact. The velocity change follows the rule of momentum conservation

$$(m\dot{x} + m_{\mathrm{b}}\dot{x}_{\mathrm{b}})_{\text{after imp}} = (m\dot{x} + m_{\mathrm{b}}\dot{x}_{\mathrm{b}})_{\text{before imp}} \tag{31}$$

where $\dot{x}_{\text{b imp}}$ and $\dot{x}_{\text{b,b imp}}$ are the velocities of the movable electrode and the mini ball before impact respectively; while $\dot{x}_{\text{a imp}}$ and $\dot{x}_{\text{b,a imp}}$ are the velocities of the two masses after the impact.

A certain amount of energy is assumed to be dissipated when the impact occurs (inelastic collision). The velocity of the movable mass and the mini-ball are given by [28]:

$$\begin{cases} \dot{x}_{\text{after imp}} = \left[\dfrac{C_{\text{ball}} m_{\mathrm{b}} (\dot{x}_{\mathrm{b}} - \dot{x}) + m\dot{x} + m_{\mathrm{b}}\dot{x}_{\mathrm{b}}}{m + m_{\mathrm{b}}}\right]_{\text{before imp}} \\ \dot{x}_{\text{b,after imp}} = \left[\dfrac{C_{\text{ball}} m (\dot{x} - \dot{x}_{\mathrm{b}}) + m\dot{x} + m_{\mathrm{b}}\dot{x}_{\mathrm{b}}}{m + m_{\mathrm{b}}}\right]_{\text{before imp}} \end{cases} \tag{32}$$

where C_{ball} is the restitution coefficient of the impact. The kinetic energy loss during the impact is given by:

$$\Delta E = \frac{1}{2}\frac{m m_{\mathrm{b}}}{m + m_{\mathrm{b}}}\left(1 - C_{\text{ball}}^2\right)\left[(\dot{x} - \dot{x}_{\mathrm{b}})^2\right]_{\text{before imp}} \tag{33}$$

V. Device Model: Numerical

A. Time-Series Recursion

To solve the kinematic equations in section III.A, we apply a simple time-series recursion method. The time is discretized into an arithmetic sequence $\{t_1, t_2, \cdots, t_i, \cdots\}$ with a constant time step of Δt, which is about two orders of magnitude smaller than the period of the excitation vibration. At a given time t_i, the status of the device (the ith status) is described as a vector $\left(x_i, \dot{x}_i, q_i, x_{\mathrm{b},i}, \dot{x}_{\mathrm{b},i}\right)$. The kinematic equations of the two masses during the next time step is predicted, according to the range of $x_{\mathrm{p},i}$ and $x_{\mathrm{b},i}$. A predictor-corrector method [29] is used for calculation of the series of status. A prediction of the $(i+1)$th status of the device at the time t_{i+1} is achieved according to the following Euler predictors (based on first order Taylor expansions) as well as the ones in section III.A.

$$u_{\mathrm{pr}} = u_i + \dot{u}_i \cdot \Delta t \tag{34}$$

herein u stands for any element of the vector $(x, \dot{x}, q, x_{\mathrm{b}}, \dot{x}_{\mathrm{b}})$.

If the kinematic equations corresponding to the predicted status at t_{i+1} are the same as the ones of the time t_i, there is no impact or separation within the time slot Δt. The next status is obtained according to the kinematic equations and the trapezoidal correctors shown below:

$$u_{i+1} = u_i + \left(\dot{u}_i + \dot{u}_{i+1,\mathrm{pr}}\right) \cdot \frac{\Delta t}{2} \tag{35}$$

If any impact or separation occurs in the time slot Δt, the kinematic equations are piecewise with time and needs a higher resolution of time step to minimize the error. Similar situations also occur when the displacement of the movable mass is high, when the air damping force is strongly affected even with slight changes of position and velocity. Under these conditions, the model switches to a smaller time step $\mathrm{d}t = \Delta t/10$ to proceed a more accurate calculation.

B. Setting Displacement When Impacts Occur

To avoid the Zeno phenomenon [30] during the velocity calculations regarding impacts, as long as at least one impact occurs during the specific time slot according to the criteria in eq. (26), we introduce an arbitrary correction of the position of the movable masses after the impact, where the after-impact position of the movable electrode is set to the maximum displacement $G \cdot \mathrm{Sgn}\left(x_{\mathrm{pr}}\right)$. In case that the movable electrode impacts with the fixed electrodes, the displacements corresponding to the beginning of the next time step x_{next} and $x_{\mathrm{b,next}}$ are set as:

$$\begin{cases} x_{\mathrm{next}} = G \cdot \mathrm{Sgn}\left(x_{\mathrm{pr}}\right) \\ x_{\mathrm{b,next}} = x_{\mathrm{b,pr}} \end{cases} \tag{36}$$

In case that the impact with the ball occurs, the displacements corresponding to the beginning of the next time

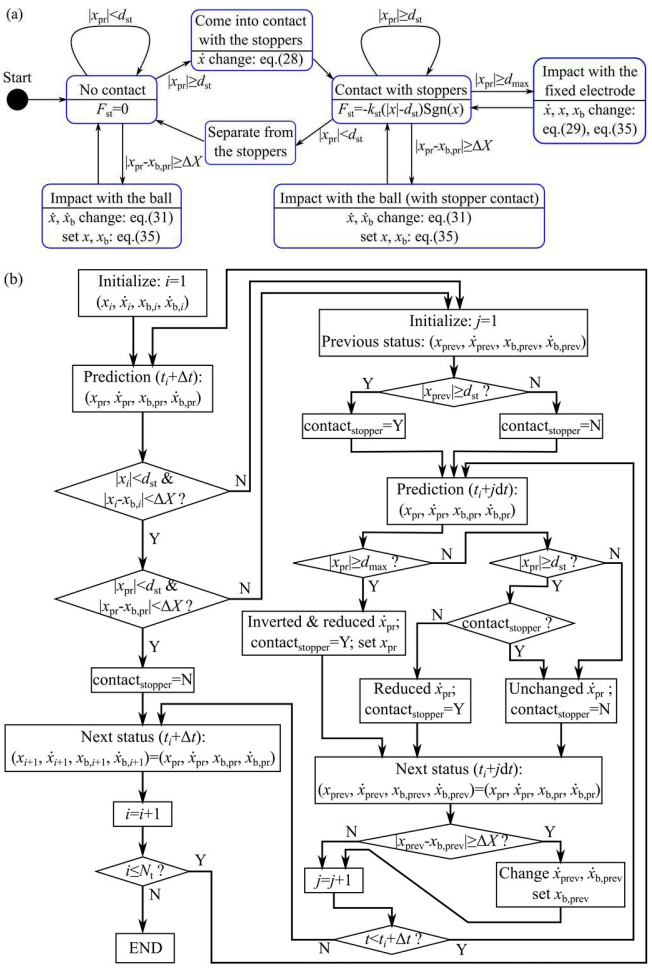

Fig. 7. (a) Diagram of state transition of the prototype. (b) Flow chart of the prototype modeling to illustrate the process of calculation.

step x_{next} and $x_{b,next}$ are set as:

$$\begin{cases} x_{\text{next}} = x_{\text{pr}} \\ x_{\text{b,next}} = x_{\text{pr}} + \Delta X \cdot \text{Sgn}\left(x_{\text{b,pr}} - x_{\text{pr}}\right) \end{cases} \tag{37}$$

C. Status Transition and Flow Chart

A diagram of the status transition of the prototype and a global flow chart of the model are shown in fig 7 to illustrate the process of calculations in the model.

VI. Experimental Validation

In order to validate the solidity of the model, the experimental measurements we presented in [23] are taken as reference for comparison with the predictions of the model. The performance chosen for comparison is the energy conversion of the prototype during each cycle of excitation in regard to changing frequencies when the device works with an optimal resistive load.

A. Experimental Setup

In the experiments, the prototype is excited by a vibrator that is controlled by a closed-loop system. Accelerations with constant amplitudes and varying frequencies (linearly increasing or decreasing with time) are applied to the prototype by the vibrator. The prototype is biased by a DC voltage of 20 V, and connected to the optimal resistive load of 6.6 MΩ (obtained experimentally). The output signal across the load resistor is recorded, and the output energy during each cycle of excitation is calculated accordingly [20]. The values of acceleration tested for frequency sweeps include 0.5 g_{peak}, 1 g_{peak} and 2 g_{peak}, while the prototype is operated with and without the ball respectively.

B. Modeling Parameters

The parameters in the model described in the previous section are sorted into several categories. Most parameters are physical constants that are known and unchanged, such as the permittivity of materials (ε_0, ε_r) and the dynamic viscosity of air (μ). Another category are the design parameters that can be determined directly by the layout or choice of components and is easy to control, such as the initial gap between electrodes (d_{init}) and the radius of the mini-ball (r). There are also parameters related to and confined by the fabrication process or experiments, such as the over-etch sidewall angle (α) and the parasitic capacitance brought by the measurement electronics (C_p). These parameters can be determined only after a first trial of fabrication [20]. In addition, parameters like the stiffness of elastic structures (k, k_{st}) and the mass of the movable electrode (m) are not only determined by the layout design but also affected by the over-etch during fabrication. There are a few parameters (such as c_{imp}) needed to be adjusted according to the measurements proceeded on a first-trial prototype, and can be kept the same for future optimizations.

The parasitic capacitance is introduced by the fringe-effect of the capacitive structure, the packaging of the device, the input channel of a signal follower and a PCB testbench shared by dynamic capacitance and power measurement setup. It acts as an additional capacitance in parallel with the device capacitance (unchanged with device motion), which can be obtained experimentally. The collision conditions affect the parasitic capacitance, mainly through the "fringe-effect" component. However, this varying component is only a minor contributor of the total parasitic capacitance. The parasitic capacitance is thus regarded as an estimated constant both experimentally and in simulation.

To determine the value of the parasitic capacitance, we measured a fixed capacitor by two tools respectively: an impedance meter and the dynamic capacitance measurement setup, which is discussed in detail in [20]. The difference of the values acquired by the two methods corresponds to the parasitic capacitance of the experimental setup, as stated in [20]. In this article, we use the previously achieved value (28 pF) of the total parasitic capacitance of our PCB testbench with an amplifier OPA445BM.

The sidewall angle can be accurately determined only by destroying the device and observing the dimensions on a cross-section cut. Even though this destructive method is not preferable, we applied the sidewall angle obtained in [31] (1.005°)

TABLE II
PARAMETERS APPLIED IN THE PROPOSED MODEL.

Quantity	Symbol	Value
Total stiffness of linear springs	k	40.5 N/m
Position of stoppers (with Parylene C)	d_{st}	66 µm
Total stiffness of elastic stoppers	k_{st}	1.02×10^4 N/m
Over-etch sidewall angle	α	1.055°
Restitution coefficient (stoppers)	c_{stop}	0.9
Restitution coefficient (ball)	c_{ball}	0.9
Friction coefficient (framework)	μ_f	1×10^{-3}
Parasitic capacitance	C_p	28 pF
Frequency sweep	$[f_{min}, f_{max}]$	[10 Hz, 170 Hz]
Time step	Δt	20 µs
Number of time steps	N_t	8×10^6
Smaller time step	dt	2 µs

as an approximation because we apply the same etching technique. A more flexible method could be to adjust the sidewall angle to fit with the capacitance variation curves of the device, which is obtained through a dynamic technique introduced in [32]. However, since the technique is less accurate when the capacitance variation is fast, the maximum capacitance is not accurate, which makes this method still unreliable for now. A list of key parameters used in the model is shown in table II.

C. Predictions of the Model

In order to validate the proposed model, the predictions given by the simulation using the parameters stated above are compared with experimental results. The simulation is proceeded both with and without the tungsten miniature ball under the excitation of frequency-sweeping accelerations (sweep-up). The time resolution of the simulation is 20 μs/2 μs, while the size of the time series for simulation has up to 8×10^6 elements. Series of accelerations with linearly changing frequency are generated with amplitudes 0.5 g_{peak}, 1 g_{peak} and 2 g_{peak} respectively as for the experiments, corresponding to the sweeping rate of about 1 Hz/s. The frequency sweeps from 10 Hz up to 170 Hz. The predictions of the model are compared with the experimental results, as shown in fig 8.

All the parameters adjusted according to the measurements, and kept unchanged for all levels of excitations once determined. For example, the stiffness of the springs is firstly predicted by a rough estimation given by FEM simulation, and slightly adjusted according to the resonance frequency of the KEH without ball under 0.5 g_{peak} acceleration, considering the geometry of the etched structure caused by the fabrication. Once the resonant frequency is matched, the spring stiffness is kept constant for the simulations of all levels of acceleration, for cases both without and with the miniature ball. Other parameters requiring adjustment include the stiffness of the stopper beam and the friction coefficient of the ball. The model can be considered as a predictive model.

It is observed that the energy conversion performance of the device versus frequency sweeps can accurately predict by the model, either without or with the ball. The error of the prediction for the working frequency range is 2 Hz with 0.5 g_{peak} acceleration, and is less than 10 Hz with 2 g_{peak} acceleration. Generally speaking, the prototype is wideband

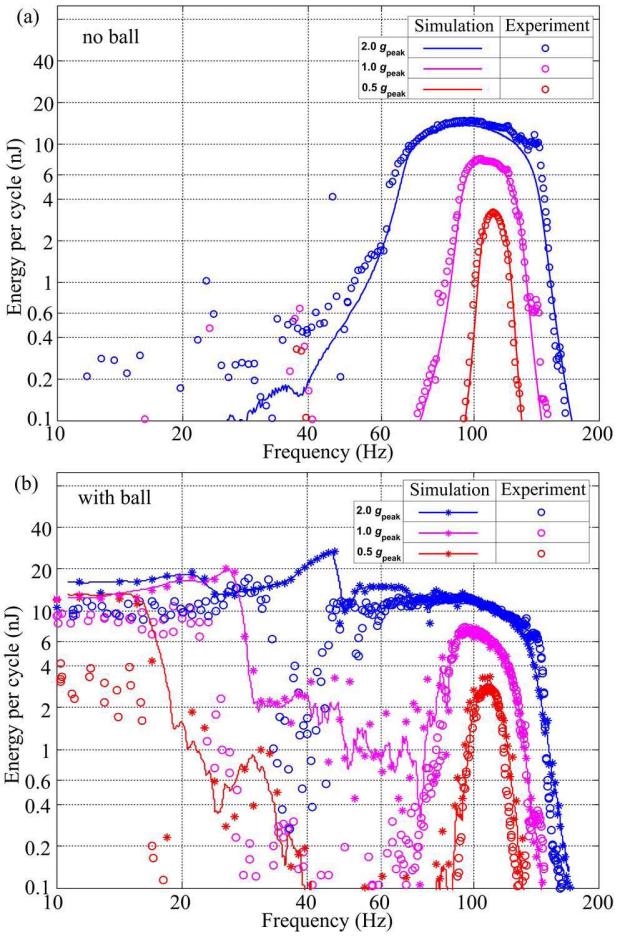

Fig. 8. Simulated and measured output power of the prototype in air with frequency sweeps: (a) without the mini-ball; (b) with the mini-ball.

either with or without the mini-ball. The mini-ball improves the energy transduction performance mainly at low frequency (<50 Hz), because of frequency up-conversion of the ball vibrating energy transferred to the moving electrode.

The resonance frequency of the spring-mass system is about 110 Hz, which is observed from the frequency response of the device without the ball with 0.5 g_{peak} acceleration. With increased accelerations, the range of working frequency is expanded, resulting from the spring softening effect of the electrostatic force and the stiffening effect of the elastic stoppers and the air damping. With the acceleration of 2 g_{peak}, a tiny peak of power is observed at 35 Hz in the frequency response of the prototype without ball, which results from a frequency up-conversion behavior brought by impacts on the elastic stoppers.

The insertion of mini-ball brings an additional working frequency band (below 40 Hz). This makes the device much more efficient for low frequency applications. Between the two working regions, the output power of the prototype is unstable, because within the range of 40-60 Hz, the oscillation of the movable electrode is occasionally interrupted by the ball. The power prediction is less accurate than that of the range of working frequency. With 2 g_{peak} 28 Hz excitation, for example, the energy conversion of the prototype (with ball) is predicted

to be 20 nJ/cycle, and is measured as 15 nJ/cycle. This error comes from the underestimation of damping during impacts between the movable electrode and the ball. Despite this, the proposed model is overall very useful for the performance evaluation in parametric studies of gap-closing prototypes suffering from large nonlinear air damping forces. A chronogram of the different forces on the movable electrode vs time when the device is working with the acceleration of 100 Hz 2 g_{peak} is attached as the supplementary material (fig. S1), illustrating the contribution of each component.

VII. Parametric Study

We carried out several parametric studies on some key design parameters, the results and analyses are presented as follows. All simulations are performed with an acceleration of 1 g_{peak} and a bias voltage of 20 V (except for fig. 9f, where the bias voltage is varied)

A. Cavity Length

The influence of cavity length (L_{cav}) on the prototype's frequency response is shown in fig 9a. With an increased cavity length, the mass of the movable electrode is slightly reduced, leading to a higher resonance frequency. At the same time, the lower band in the frequency response of the prototype is shifted towards even lower frequency. The reason for this is that the time required by the ball to travel between the two ends of the cavity is longer with a longer cavity given fixed amplitude of excitation. In summary, the entire frequency response is widened with a larger cavity length.

B. Initial Gaps of the Stoppers

Shown in fig 9b is the influence of the initial gap of the stoppers on the frequency response of the KEH. One of the major functions of the stoppers is to prevent pull-in, which is strongly related to their initial gap. The position of the stoppers is strongly related to the pull-in voltage. With the bias voltage of 20 V, the pull-in occurs when $g_{\text{st}} = 69\ \mu$m (corresponding to a gap of 1 μm between combs' fingers at the stoppers' impact point).

When the initial gaps of the stoppers vary from $g_{\text{st}} = 68\ \mu$m to $g_{\text{st}} = 62\ \mu$m, the output power between 10 Hz and 25 Hz is reduced by 67%, which is due to the reduced $C_{\max}$ caused by an enlarged minimum gap between electrodes.

Another function of the stoppers is to bounce the movable electrode back when the external oscillation is far lower than the resonance, so that a mechanical frequency up conversion oscillation is reached. The damping of the stoppers' impacts is negligible compared to the air damping, so that the oscillation can sustain during the time interval between two triggering behaviors (impacts on the ball).

C. Stiffness of Elastic Structures

The KEH behavior with varied stiffness of the serpentine springs (k_1) and the one of the elastic beams (k_2) in the stoppers can be observed from fig 9c-d respectively.

The influence of k_1 is obvious: by lowering it, the frequency response of the prototype is shifts downwards in the frequency domain. This is beneficial for the applications of low frequencies. However, a lower spring force also means that the pull-in will occur at a lower voltage.

The elastic beams are very important to keep the device from the pull-in status, because it offers an additional force acting against the electrostatic attraction. The influence of their stiffness to the power performance of the KEH is negligible, as long as it is high enough to keep the movable electrode from pull-in. The reason for this is that the k_2 that prevents pull-in is far larger than the one of the linear springs, and the deformation of elastic beams are usually negligible.

The energy loss from air damping is quite huge compared to the one of the stoppers' impacts, and the latter is related to k_2. Technically, we tend to design elastic stoppers with high stiffness as long as they lead to low impact losses.

D. Initial Gaps Between Combs' Fingers

Fig. 9e shows the effects brought by a varied initial gap between combs' fingers at rest. Provided that the initial gap at rest is smaller, its influences on the power output are generated through two routes. On the one hand, there will be room for more comb fingers which leads to a larger maximum capacitance, with positive influence on the power output. This effect is clearly observed at low frequency (below 25 Hz).

With a small initial gap (50 μm), the electrostatic force is large, leading to a strong spring-softening effect, and expanding the resonance peak towards the low frequency (from 100 Hz to 60 Hz). If the initial gap is below 50 μm, the electrodes tend to be trapped in pull-in status due to the large electrostatic attraction.

On the other hand, the air damping of the KEH with more fingers is larger, confining the capacitance ratio ($C_{\max}/C_{\min}$) and consequently the output power at high frequency (around 100 Hz).

E. Bias Voltage

The power of the KEH is greatly influenced by the bias voltage between electrodes, as shown in fig 9f. With an increased bias voltage, the electrostatic force is increased, leading to a stronger spring softening effect. Thus, the resonance frequency moves downward, and the range of working frequency widens. Furthermore, both the amount of converted energy and the efficiency are increased dramatically. However, the risks of pull-in events are growing with the increasing bias voltage: the oscillation of the movable mass is more easily stopped by the electrostatic force with low acceleration. There is no pull-in event with 20 V bias, but with 30 V bias, the device is easily interrupted by pull-in with the 1 g_{peak} acceleration. In order to compensate this disadvantage, the stiffness of the spring should be increased so as to avoid the pull-in.

VIII. Discussions

According to the parametric study of the KEH, we observe that to achieve optimal performances, we should usually adjust several design parameters simultaneously. Several issues must be taken into account including the pull-in, the modeling of

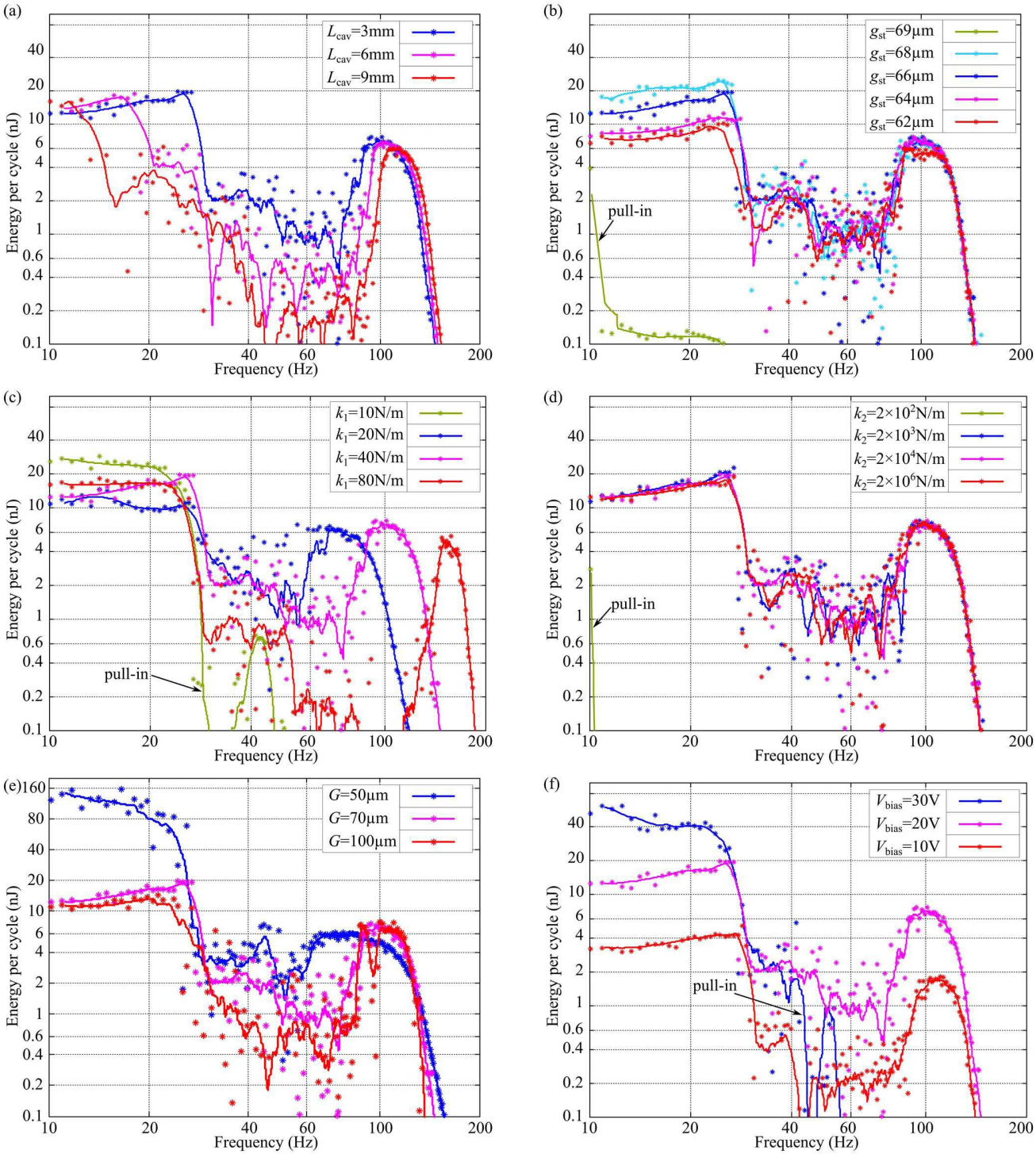

Fig. 9. Simulation results of parametric studies: influences of (a) cavity length; (b) stopper position; (c) stiffness of serpentine springs; (d) stiffness of elastic stoppers; (e) initial gap at rest; (f) bias voltage on the frequency-dependent power responses of the KEH with 1 g_{peak} acceleration.

the mini-ball motions, and the overlapping influence of some parameters.

A. Pull-In

The output power of the proposed capacitive KEH is determined by the capacitance variation and the bias voltage. Both a high bias voltage and a large range of capacitance variation are preferable for maximizing the output power of the prototype. However, both these factors will give rise to a larger electrostatic force, and if the electrostatic force is overwhelming, the movable structure will be trapped in the status of pull-in. This means that the movable electrode is strongly attracted by the fixed electrodes, and cannot reach high displacement even when excited by a large acceleration.

In order to avoid pull-in, the capacitance variation and the bias voltage must be confined under certain limits. With the help of the proposed model, we can easily find out these limits.

The air damping is another factor that counteracts the electrostatic force, and thus increases the pull-in voltage. The more accurate modeling of air damping effect can thus help us achieve a better accuracy in the prediction of pull-in voltage in the prototypes.

B. Mini-Ball Motion Modeling

The present model is capable to predict the frequency up conversion behavior of the KEH and to indicate the change of power with various design parameters. However, the level of simulated power at low frequencies (below 25 Hz) is generally higher than the experimental measurements. In the proposed model, we suppose that a constant restitution coefficient corresponding to the loss of kinetic energy during the impact between the ball and the movable mass. In addition, the rotation of the ball is not taken into account. This can explain the differences between simulations and the experiments.

C. Parameters With Overlapping Influences

From fig. 9 we observe the influences of parameters on the KEH's frequency response overlap with each other. Simultaneously, the effects of changing a single design parameter include changes of the several aspects of the frequency response. For instance, the low frequency power is influenced not only by the bias voltage, but also by the initial gap between electrodes and the stopper position. While an increased cavity length results in not only a higher resonance frequency, but also a lower dropping frequency of the low frequency band. This means that if we want to adjust a single aspect of the frequency curves, we must always co-adjust several design parameters simultaneously.

D. Simplified Model for Impact Forces

For simulation purposes, we have simplified the model of the impact force: the impact force between the movable electrode and the mini-ball is effective only at the impacting point, because the impact time is far less than the time step dt thanks to the rigidity of the two impacting components. Thus, what really matters is how much energy is dissipated in this near-instantaneous collision, which is captured in the restitution coefficient (0.9).

Admittedly, the fact that this coefficient should be assessed from experimental (system-level) characterization results may be considered a weak point of our model. One may then try to improve on the impact model, by determining *a priori* the value of the restitution coefficient. Whether this can be achieved without recourse to characterization is arguable. In fact, as shown by a survey of the literature, predictive models of dissipative contact (i.e. friction) at the micro-scale need an accurate knowledge of the roughness of the surfaces in contact (typ. distribution of height and radius of curvature of asperities), which may only be achieved through even finer and costlier characterization than we have performed (e.g. AFM characterization of surface roughness).

IX. Conclusion

In this article we propose a model that describes the frequency performance of a gap-closing kinetic energy harvester with impact-coupled mechanical frequency up conversion mechanism. The model is based on a time domain finite difference method, with adaptive time steps. It takes into account all the impacts and the thin-film air damping within the prototype, and is a fully predictive model that can be applied for the simulation of future designs. The model provides simulation results that fits previous experimental characterization. Once established, it can be used as a convenient tool for designing a fully optimized in-plane gap-closing capacitive KEH without additional fabrications and characterizations.

1) The non-linear squeeze film air damping effect in the MEMS e-KEH with gap-closing structures of high aspect ratio is modeled in a predictive way based on physical principles rather than post-fabrication fittings. The model is thus capable of performing simulations consistent with the experimental results regardless of the excitation level.
2) The predictions of the model are validated through comparing with experimental results, showing a good consistency with the measurements. The output power around resonance frequency (100 Hz) is accurately predicted by the model, but is overestimated by the model at low frequency (below 25 Hz).
3) Parametric study is carried out on the basis of the proposed model. The influences of different design parameters to the device's frequency response are simulated and analyzed, including the cavity length, stopper position, stiffness of the elastic structures, initial gap between electrodes, and the bias voltage. Accordingly, the basic design rules are summarized.
4) According to the parametric studies, we can conclude the following rules:
    a) The stiffness of the elastic stoppers should be as high as possible, as long as it ensures low energy loss during impact.
    b) A smaller initial gap between two electrodes is beneficial for increasing the low frequency power of the KEH, as long as pull-in does not take place.
    c) A larger bias voltage, a smaller stiffness of the linear springs, and a larger initial at the stoppers are preferable, because they all lead to a larger power. However, their limit is to avoid pull-in.

In summary, we have proposed a model that is able to predict the behavior of a KEH with gap-closing interdigital combs, based on a set of parameters adjusted according to experimental measurements and remaining constant for varied experimental conditions. The model considers the highly nonlinear squeeze film air damping effect in the MEMS device with air gap of high aspect ratio, which ensures the high accuracy of the simulation. From the predictions, we find several design rules for the future designs. The cavity length is a key parameter that affects the frequency performance of the prototype at low frequency. As for optimizing the power performance, the bias voltage and the stopper position are the two factors that need joint adjustment. The stiffer elastic beams

are preferable as long as it ensures low loss during impact. While a higher stiffness of the linear springs is beneficial, since it allows larger pull-in voltage and enhances the reliability of the prototype, and the low frequency output power is not strongly affected.

ACKNOWLEDGMENT

The authors would like to give their thanks to Dr. Frédéric Marty for his help in the fabrication of the proposed design.

REFERENCES

[1] C. Shearwood and R. B. Yates, "Development of an electromagnetic microgenerator," *Electron. Lett.*, vol. 33, no. 22, pp. 1883–1884, Oct. 1997.
[2] F. Cottone, H. Vocca, and L. Gammaitoni, "Nonlinear energy harvesting," *Phys. Rev. Lett.*, vol. 102, no. 8, p. 080601, 2009.
[3] B. Cavallier, P. Berthelot, H. Nouira, E. Foltete, L. Hirsinger, and S. Ballandras, "Energy harvesting using vibrating structures excited by shock," in *Proc. IEEE Ultrason. Symp.*, vol. 2, Sep. 2005, pp. 943–945.
[4] T. Galchev, H. Kim, and K. Najafi, "A parametric frequency increased power generator for scavenging low frequency ambient vibrations," *Procedia Chem.*, vol. 1, no. 1, pp. 1439–1442, 2009.
[5] K. Tao, L. Tang, J. Wu, S. W. Lye, H. Chang, and J. Miao, "Investigation of multimodal electret-based MEMS energy harvester with impact-induced nonlinearity," *J. Microelectromech. Syst.*, vol. 27, no. 2, pp. 276–288, 2018.
[6] X.-S. Zhang *et al.*, "Frequency-multiplication high-output triboelectric nanogenerator for sustainably powering biomedical microsystems," *Nano Lett.*, vol. 13, no. 3, pp. 1168–1172, 2013.
[7] A. Paracha, P. Basset, P. Lim, and F. M. Bourouina, "A bulk silicon-based vibration-to-electric energy converter using an in-plane overlap plate (IPOP) mechanism," in *Proc. Workshop PowerMEMS*, 2006, pp. 1–4.
[8] Y. Naruse, N. Matsubara, K. Mabuchi, M. Izumi, and S. Suzuki, "Electrostatic micro power generation from low-frequency vibration such as human motion," in *Proc. PowerMEMS*, 2008, pp. 19–22.
[9] S. Cheng and D. Arnold, "A multi-pole magnetic generator with enhanced voltage output for low-frequency vibrational energy harvesting," in *Proc. PowerMEMS*, Sendai, Japan, Nov. 2008, pp. 125–128.
[10] P. Pillatsch, E. M. Yeatman, and A. S. Holmes, "A scalable piezoelectric impulse-excited energy harvester for human body excitation," *Smart Mater. Struct.*, vol. 21, no. 11, p. 115018, 2012.
[11] M. Han, X. Zhang, W. Liu, X. Sun, X. Peng, and H. Zhang, "Low-frequency wide-band hybrid energy harvester based on piezoelectric and triboelectric mechanism," *Sci. China Technol. Sci.*, vol. 56, no. 8, pp. 1835–1841, 2013.
[12] S. Meninger, J. O. Mur-Miranda, R. Amirtharajah, A. Chandrakasan, and J. H. Lang, "Vibration-to-electric energy conversion," *IEEE Trans. Very Large Scale Integr. (VLSI) Syst.*, vol. 9, no. 1, pp. 64–76, Feb. 2001.
[13] R. Guilllemet, P. Basset, D. Galayko, F. Cottone, F. Marty, and T. Bourouina, "Wideband MEMS electrostatic vibration energy harvesters based on gap-closing interdigited combs with a trapezoidal cross section," in *Proc. IEEE 26th Int. Conf. Micro Electro Mech. Syst. (MEMS)*, Jan. 2013, pp. 817–820.
[14] Y. Suzuki, M. Edamoto, N. Kasagi, and K. K. Morizawa, "Micro electret energy harvesting device with analogue impedance conversion circuit," in *Proc. PowerMEMS*, 2008, pp. 1–4.
[15] D. Galayko *et al.*, "Capacitive energy conversion with circuits implementing a rectangular charge-voltage cycle—Part 1: Analysis of the electrical domain," *IEEE Trans. Circuits Syst. I, Reg. Papers*, vol. 62, no. 11, pp. 2652–2663, Nov. 2015.
[16] K. Tao *et al.*, "A novel two-degree-of-freedom MEMS electromagnetic vibration energy harvester," *J. Micromech. Microeng.*, vol. 26, no. 3, p. 035020, 2016.
[17] J. Li, C. Xu, J. Tichy, and D. A. Borca-Tasciuc, "A one-dimensional model for design and predicting dynamic behavior of out-of-plane MEMS," *J. Micromech. Microeng.*, vol. 28, no. 8, p. 085021, 2018.
[18] Y. Feng, B. Shao, X. Tang, Y. Han, T. Wu, and Y. Suzuki, "Improved capacitance model involving fringing effects for electret-based rotational energy harvesting devices" *IEEE Trans. Electron Devices*, vol. 65, no. 4, pp. 1597–1603, Apr. 2018.
[19] Y. Lu, F. Cottone, S. Boisseau, F. Marty, D. G. Basset, and P. Basset, "A nonlinear MEMS electrostatic kinetic energy harvester for human-powered biomedical devices," *Appl. Phys. Lett.*, vol. 107, no. 25, p. 253902, 2015.
[20] Y. Lu *et al.*, "A batch-fabricated electret-biased wideband MEMS vibration energy harvester with frequency-up conversion behavior powering a UHF wireless sensor node," *J. Micromech. Microeng.*, vol. 26, no. 12, p. 124004, 2016.
[21] L. M. Miller, E. Halvorsen, T. Dong, and P. K. Wright, "Modeling and experimental verification of low-frequency MEMS energy harvesting from ambient vibrations," *J. Micromech. Microeng.*, vol. 21, no. 4, p. 045029, 2011.
[22] S. Kaur, E. Halvorsen, O. Søråsen, and E. Yeatman, "Characterization and modeling of nonlinearities in in-plane gap closing electrostatic energy harvester," *J. Microelectromech. Syst.*, vol. 24, no. 6, pp. 2071–2082, 2015.
[23] Y. Lu, F. Marty, D. Galayko, J.-M. Laheurte, and P. Basset, "A power supply module for autonomous portable electronics: Ultralow-frequency MEMS electrostatic kinetic energy harvester with a comb structure reducing air damping," *Microsyst. Nanoeng.*, vol. 4, p. 28, Oct. 2018.
[24] P. Basset, E. Blokhina, and D. Galayko, *Electrostatic Kinetic Energy Harvesting*. Hoboken, NJ, USA: Wiley, 2016.
[25] M. Bao and H. Yang, "Squeeze film air damping in MEMS," *Sens. Actuators A, Phys.*, vol. 136, no. 1, pp. 3–27, 2007.
[26] A. Brenes, B. Vysotskyi, E. Lefeuvre, and J. Juillard, "Nondestructive gap dimension estimation of electrostatic MEMS resonators from electrical measurements," *Mech. Syst. Signal Process.*, vol. 112, pp. 10–21, Nov. 2018.
[27] T. Veijola, H. Kuisma, J. Lahdenperä, and T. Ryhänen, "Equivalent-circuit model of the squeezed gas film in a silicon accelerometer," *Sens. Actuators A, Phys.*, vol. 48, no. 3, pp. 239–248, 1995.
[28] S. McNamara and W. R. Young, "Inelastic collapse and clumping in a one-dimensional granular medium," *Phys. Fluids A, Fluid Dyn.*, vol. 4, no. 3, pp. 496–504, 1992.
[29] R. W. Hamming, "Stable predictor-corrector methods for ordinary differential equations," *J. ACM*, vol. 6, no. 1, pp. 37–47, 1959.
[30] L. Yu, J.-P. Barbot, D. Benmerzouk, D. Boutat, T. Floquet, and G. Zheng, "Discussion about sliding mode algorithms, Zeno phenomena and observability," in *Proc. Int. Workshop Variable Struct. Syst.*, 2011, pp. 199–219.
[31] P. Basset, D. Galayko, F. Cottone, R. Guillemet, E. Blokhina, and F. M. Bourouina, "Electrostatic vibration energy harvester with combined effect of electrical nonlinearities and mechanical impact," *J. Micromech. Microeng.*, vol. 24, no. 3, p. 035001, 2014.
[32] P. Basset, D. Galayko, A. M. Paracha, F. Marty, A. Dudka, and T. Bourouina, "A batch-fabricated and electret-free silicon electrostatic vibration energy harvester," *J. Micromech. Microeng.*, vol. 19, no. 11, p. 115025, 2009.

Yingxian Lu received the B.S. in electronics and information engineering from Beihang University, China, in 2010, and the M.S. degree in microelectronic engineering from Tsinghua University, China, in 2014, and the Ph.D. degree from Université Paris-Est in 2018. She is currently holds a post-doctoral position with the School of Life Sciences, Tsinghua University.

Her research interests include kinetic energy harvesters for power supply applications of wireless sensor nodes or for wearable electronics, MEMS device modeling, design and characterization, RF system optimization, and flexible electronic devices. Her research is focused on capacitive kinetic energy harvesters working with ultra-low frequency vibrations or motions, including random environmental vibrations, machine vibrations, or human motions.

Jérôme Juillard was born in Nice, France, in 1973. He graduated from École Centrale Paris in 1995, with a specialization in electronics and signal processing. He received the master's degree in acoustics and signal processing from IRCAM, and the Ph.D. degree in physical acoustics from University Paris 7 in 1999.

In 2000, he joined Supélec (now CentraleSupélec), where he is currently a Full Professor. His research is conducted with the Electronic Systems Team, GEEPs Laboratory. His research interests are nonlinear oscillators and MEMS modeling, design, characterization, and test.

Francesco Cottone received the Ph.D. degree in physics from the Department of Physics and Geology, University of Perugia, Italy, in 2008. After Ph.D., he worked outside Italy in nonlinear dynamical systems for vibration energy harvesting at the Stokes Institute, University of Limerick, Ireland. In 2011, he received a Marie Curie European Fellowship for a project related to nonlinear electrostatic MEMS energy harvesting technology at ESIEE Paris, Université de Paris-Est, France.

Since 2013, he re-joined the Noise in Physical System Laboratory, Italy, where he is currently serving as a Senior Researcher and a Professor at the Department of Physics and Geology. He is involving in nonlinear micro systems and innovative electro-active materials for energy harvesting. His scientific expertise includes gravitational waves detectors, nonlinear stochastic systems, and electro-active materials for energy harvesting. He has a record of more than 50 referred publications, holds two patents, and several talks at international conferences on energy harvesting technology.

Dimitri Galayko (M12) graduated from Odessa State Polytechnich University, Ukraine, in 1998, he received the master's degree from the Institut of Applied Sciences of Lyon (INSA-LYON, France) in 1999 and the Ph.D. degree from the University Lille-I in 2002. He made his Ph.D. thesis with the Institute of Microelectronics and Nanotechnologies (IEMN, Lille, France). The topic of his Ph.D. dissertation was the design of microelectromechanical silicon filters and resonators for radio-communications.

Since 2005, he has been an Associate Professor with the LIP6 Laboratory, Sorbonne Université–University Paris-VI (Pierre et Marie Curie). His research interests include study, modeling, and design of nonlinear integrated circuits for sensor interface and for mixed-signal applications.

Philippe Basset received the Engineering Diploma in electronics from ISEN Lille, France, in 1997, the M.Sc. degree from IEMN, University of Lille, in 1999, and the Ph.D. degree from IEMN, University of Lille, in 2003, in the areas of microelectronic and micro-electro-mechanical-systems (MEMS).

In 2004, he held a post-doctoral position at CMU, Pittsburgh, USA, and he joined ESIEE Paris in 2005. He is currently a Professor at Université Paris-Est/ESIEE Paris, a member of the ESYCOM Laboratory, he is also Leading the Sensors and Measuring MEMS Group. His current research interests include micro-power sources for autonomous MEMS and micro/nano-structuration of silicon. He has been serving with the International Steering Committee of the PowerMEMS Conference since 2015.